Astronomy & Astrophysics manuscript no. main
April 24, 2026

Impact of Primordial Black Hole population on 21 cm observables at high redshift

Atrideb Chatterjee,[1⋆] Barun Maity,[2⋆⋆] and Koushiki[3]

[1] Kapteyn Astronomical Institute, University of Groningen, PO Box 800, 9700 AV Groningen, The Netherlands
e-mail: a.chatterjee@rug.nl
[2] Max-Planck-Institut für Astronomie, Königstuhl 17, 69117 Heidelberg, Germany
e-mail: maity@mpia.de
[3] International Centre for Space and Cosmology, School of Arts and Sciences, Ahmedabad University, Ahmedabad, GUJ 380009, India
e-mail: koushiki.malda@gmail.com

April 24, 2026

ABSTRACT

The 21-cm signal, one of the most promising probes of the high-redshift Universe, has traditionally been modelled without accounting for the effects of active galactic nuclei (AGN) in the pre-JWST era, primarily due to the lack of observational evidence for AGNs at $z > 6$. However, following the discovery of several AGNs at redshifts as high as $z \sim 10$ by JWST, it has become imperative to incorporate the impact of these early AGNs when predicting the 21-cm signal. Supposing that these AGNs are seeded by primordial black holes (PBHs), we study their impact with a semi-numerical model setup. Specifically, we extended the explicitly photon-conserving reionization framework, SCRIPT, including essential cosmic dawn physics and PBH contributions. This enables us to compute both the global signal and the power spectrum of the 21-cm line over the redshift range $z \sim 30 - 5$ within a self-consistent framework. Building on this setup, we then investigate the impact of different PBH mass functions (obeying current observational constraints) on the resulting signal. The X-ray heating from PBHs can substantially make the depth of the global 21-cm signal shallower and suppress the expected power amplitude during cosmic dawn. We also find that the choice of mass function plays a crucial role in shaping the 21-cm signal, and can, in fact, lead to significantly different predictions.

Key words. galaxies: high-redshift / quasars: general / cosmology: theory / dark ages / reionization / first stars

1. Introduction

The 21-cm signal, originating from the hyperfine transition of neutral hydrogen, provides a powerful probe of the early Universe ($z \sim 30 - 5$) by tracing the thermal and ionization state of the intergalactic medium (IGM) (e.g., Pritchard & Loeb 2012; Greig & Mesinger 2015; Kern et al. 2017; Greig & Mesinger 2018; Gillet et al. 2019; Mesinger 2019). Since the state of the IGM is governed by the properties of the astrophysical sources present at these epochs, the 21-cm signal is effectively determined by the properties of these early sources (e.g., Ghara et al. 2021; Chatterjee et al. 2021; Hutter et al. 2021; Trebitsch et al. 2023a).

Observationally, this signal is studied through two main aspects: (*i*) the sky-averaged global signal, and (*ii*) its spatial fluctuations, commonly characterised by the power spectrum. Except for a handful of studies in the past decade (e.g., Tashiro & Sugiyama 2013; Gong & Kitajima 2017; Mena et al. 2019; Ewall-Wice et al. 2020; Yang 2021; Mittal et al. 2022; Saha & Laha 2022; Nelander et al. 2025), both these observational aspects have historically been modelled assuming the astrophysical sources to be primarily star-forming (SF) in nature (e.g., Barkana & Loeb 2001; Furlanetto et al. 2006; Chatterjee et al. 2023; Dhandha et al. 2025; Sims et al. 2025; Gessey-Jones et al. 2025), with potentially significant contribution from active galactic nuclei (AGN) only at later times ($z \sim 5$) (Onoue et al. 2017; Dayal et al. 2020; Trebitsch et al. 2023b; Dayal et al. 2025). In fact, the few studies, mentioned earlier, that did include AGNs at early redshifts ($z > 6$), primarily aimed to explain the non-standard feature of the global 21-cm signal tentatively detected by the EDGES experiment (Bowman et al. 2018), which has since been ruled out at 95.3% confidence level by the Shaped Antenna Measurement of the Background Radio Spectrum 3 (SARAS-3) experiment (Singh et al. 2022).

In light of recent James Webb Space Telescope (JWST) observations, revealing the presence of AGNs as early as $z \sim 6 - 10$, often dubbed as Little Red Dot (Greene et al. 2024; Bogdán et al. 2024; Kovács et al. 2024; Napolitano et al. 2024; Schneider et al. 2023; Napolitano et al. 2025), necessitates a reassessment of their potential impact on the 21-cm signal (Kohri et al. 2022; Zhao et al. 2025, 2026). Assuming these early AGNs were seeded by the primordial black holes (PBHs) (Liu & Bromm 2022, 2023; Gouttenoire et al. 2024; Yuan et al. 2024; Dayal 2024; Matteri, Antonio et al. 2025; Ziparo et al. 2025; Dayal & Maiolino 2026), Chatterjee (2026, C26 hereafter) developed a framework to incorporate the additional contribution of such PBH-seeded early AGNs in predicting the global 21-cm signal. We showed that these exotic objects can have a considerable impact on the global signal. Nevertheless, C26 model had two key limitations: (*i*) it could only predict the globally averaged 21-cm signal but not its

⋆ Corresponding Author.
⋆⋆ A. Chatterjee and B. Maity contributed equally to this work.

fluctuations, i.e., 21-cm power spectrum, due to its analytic nature, and (*ii*) the global signal was computed under the assumption that PBHs follow a log-normal mass function.

The aim of this work is to address both of these limitations. First, we extend the C26 formalism to compute not only the global 21-cm signal but also the corresponding power spectrum. Second, we use this extended framework to investigate the impact of different PBH mass functions on the 21-cm signal.

To this end, we employ the Semi-numerical Code for ReIonization with PhoTon Conservation (SCRIPT), which incorporates a self-consistent treatment of inhomogeneous recombinations, the thermal evolution of the intergalactic medium (IGM), and radiative feedback effects during the epoch of reionization (EoR) (Maity & Choudhury 2022a). We further extend this framework to include key Cosmic Dawn (CD) processes, such as X-ray heating and Ly-α coupling, and incorporate the contribution from PBHs. This enables a unified treatment of IGM evolution across both the CD and the EoR, accounting for the effects of star-forming as well as PBH-seeded galaxies.

This work is crucial given the ongoing and planned experiments to detect the 21-cm signal. While SARAS-3 (Singh et al. 2022), SCI-HI (Voytek et al. 2014), the Broadband Instrument for Global Hydrogen Reionisation Signal (BIGHORNS; Sokolowski et al. 2015), the Radio Experiment for the Analysis of Cosmic Hydrogen (REACH; Cumner et al. 2022), and the Cosmic Twilight Polarimeter (CTP; Nhan et al. 2018) are primarily focused on measuring the global signal, experiments such as the Low Frequency Array (LOFAR; van Haarlem et al. 2013; Mertens et al. 2025), the Murchison Widefield Array (MWA; Tingay et al. 2013; Nunhokee et al. 2025), the Giant Metrewave Radio Telescope (GMRT; Paciga et al. 2013), the Hydrogen Epoch of Reionization Array (HERA; DeBoer et al. 2017; HERA Collaboration et al. 2023), and the New Extension in Nançay Upgrading LOFAR (NenuFAR; Munshi et al. 2024) are targeting the 21-cm power spectrum. Furthermore, the upcoming major facilities like SKA-low (AA* and AA4 configuration) are expected to detect the fluctuation amplitude with percentage level precision, along with providing a tomographic map of the 21 cm signal.

Throughout this paper, we adopt a ΛCDM model with dark energy, dark matter and baryonic densities in units of the critical density as $\Omega_\Lambda = 0.691$, $\Omega_m = 0.308$ and $\Omega_b = 0.0482$, respectively, a Hubble constant $H_0 = 100h\,\mathrm{km\,s^{-1}\,Mpc^{-1}}$ with $h = 0.678$, spectral index $n_s = 0.961$ and normalisation $\sigma_8 = 0.829$ (Planck Collaboration et al. 2016).

The paper is organised as follows - Sec. 2 describes different PBH mass functions and the semi-analytical model of the early AGNs seeded by these PBHs. While Sec. 3 describes the model and the simulation setup for SF galaxies, Sec. 4 presents the calculation of the 21-cm signal obtained from the contribution of both AGNs and SF galaxies. Sec. 5 describes the findings and finally, we summarise our results and conclusion in Sec. 5.

2. PBH mass functions and the early AGNs

2.1. PBH mass functions

The discussion of the occurrence of BHs at a very early age of the universe started with the works of Hawking and Carr (Hawking 1971; Carr & Hawking 1974). They showed that BHs can form soon after the big bang ($\sim 10^{-47}s$), and thus their production mechanism is very plausibly driven by inflationary potentials (Koushiki et al. 2025b; Mosani et al. 2023) or phase transitions (Carr & Kuhnel 2020). Depending on whether the production mechanism follows inflationary or phase transitions, their mass function would be different (Yokoyama 1998; Musco et al. 2024). In fact, even within an inflationary production mechanism, different inflationary potentials (Linde 1983; Lucchin & Matarrese 1985; Albrecht & Steinhardt 1982) could lead to different PBH mass functions. In view of this large number of plausible PBH mass functions, we choose some physically motivated selection criteria and only calculate the 21-cm signal from those mass functions that follow those criteria.

The selection criteria are given below

1. The formation of the PBHs, giving rise to the specific mass functions, must be triggered by a viable physical process. For instance, the mass function could arise from the density fluctuations (Dolgov & Silk 1993), or from phase-transitions (Choptuik 1993; Koushiki et al. 2025a). Note that there are multiple mass functions which are phenomenologically motivated (Dienes et al. 2025; Chen et al. 2016), but are not associated with a particular formation or collapse scenario. The latter category of mass functions is not physically motivated and therefore is not considered in this work.
2. These number densities must also abide by observational constraints coming from spectral index distortion in CMB, low-scale lensing (micro, nano, femto) experiments and accretion constraints (Carr et al. 2010). The distributions, considered here, abide by these constraints (Carr et al. 2017; Carr et al. 2021; Carr & Green 2024).
3. The number densities from these mass functions must also remain high enough throughout the observational history for their abundance to be significant, even post-evaporation Carr et al. (2021); Carr & Kuhnel (2025).

Among the set of plausible mass functions, only three distributions abide by all the constraints listed above. These PBH mass functions are briefly discussed below:

– **Log-normal mass function:** In this case, PBHs are largely anticipated to originate from primordial fluctuations in space-time (Krasnov & Nikulin 2023). Dolgov & Silk (1993) proposed such a fluctuation of Baryons producing higher densities at small scales and lower densities at larger scales. The small patches of such overdensities generate the fluctuations, which in turn produce PBHs with a mass function given by:

$$\frac{dN}{dM_{\rm PBH}} = \frac{\kappa_{LN}}{\sqrt{2\pi}\sigma M_{\rm PBH}^2}\exp\left(-\frac{\ln\left(M_{\rm PBH}/M_{\rm crit}\right)^2}{2\sigma^2}\right), \tag{1}$$

where, $M_{\rm PBH}$ is the mass of the PBH seed, $\kappa_{\rm LN}$ is the normalisation constant, and σ is the deviation around the critical mass $M_{\rm crit}$. We fix $\sigma = 0.7$ (Matteri, Antonio et al. 2025), and $M_{\rm crit} = 10^{3.65}M_\odot$, the average mass of the PBH seed (C26).

– **Power-law mass function:** Carr (1975) proposed another model of density fluctuation that changes as the effective equation of state of the universe changes. In this scenario, the fluctuation is added on top of an FLRW universe. This specific form of fluctuation gives rise to the mass function:

$$\frac{dN}{dM_{\rm PBH}} = \kappa_{\rm PL}M_{PBH}^{-\alpha}, \tag{2}$$

where, κ_{PL} is the normalisation constant and $\alpha = \frac{2(1+2\omega)}{(1+\omega)}$ with ω being the equation of state of the universe. In this

work, we assume that the PBH seeds are produced at the matter-dominated epoch, making $\omega = 0$, which produces $\alpha = 2$.

– **Critical mass function:** There is a series of numerical works that showed with different one-parameter scalar field families, the collapse which forms a zero mass BH if the parameter attains a critical value (Choptuik 1993; Gundlach 1997; Koushiki et al. 2025a). Later, this mechanism was used to explain the formation of PBHs via phase transitions (Yokoyama 1998; Musco & Miller 2013) that produce mass function (Carr et al. 2017):

$$\frac{dN}{dM_{\rm PBH}} = \kappa_{\rm CL} M_{\rm PBH}^{1.85} \exp\left[-\left(\frac{M_{\rm PBH}}{M_{\rm H}}\right)^{2.85}\right], \tag{3}$$

where, $\kappa_{\rm CL}$ is the normalisation constant and M_H is the Hubble horizon mass, given by $M_H \equiv \frac{c^3 t_{crit}}{GM_\odot} = 2.03 \times 10^4 \left(\frac{t}{0.1\,\rm s}\right) M_\odot$ (Carr et al. 2021). We have fixed $t = 0.1$ sec.

We fix the normalisation constants $\kappa_{\rm LN}$, $\kappa_{\rm PL}$ and $\kappa_{\rm CL}$ such that the comoving number density of the PBHs matches with the observed values of $10^{-5.27}$ cMpc^{-3} at $z \sim 10$ (Kovács et al. 2024; Bogdán et al. 2024) for a PBH seed with mass $10^{4.65} M_\odot$. The values for the normalisation constants come out to be 4.4×10^{-8}, 2.3×10^{-1}, and 4.2×10^{-15} for Log-normal, Power-law, and Critical mass functions, respectively.

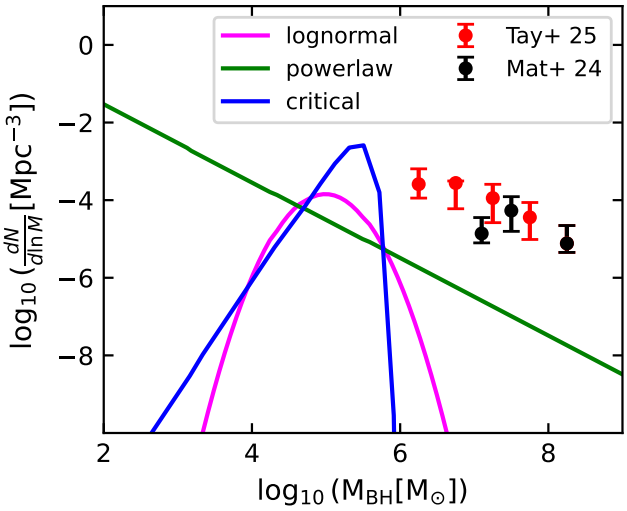

Fig. 1. Mass functions obtained for Different PBH models at $z \sim 5$ along with the recent JWST estimates (Matthee et al. 2024; Taylor et al. 2025). The magenta, green, and blue lines correspond to power-law, log-normal, and critical mass functions, respectively. Further, the black points with error bars are from Matthee et al. (2024), whereas the red ones are taken from Taylor et al. (2025). Since we do not add the contribution from astrophysically produced AGNs, all the PBH models produce mass functions that are 2-3 orders of magnitude lower than the observed values.

2.2. Semi-analytical Model for early AGNs

In order to describe the formation and evolution of the early-AGNs seeded by these PBHs, we closely follow the PHANES framework (Dayal & Maiolino 2026), which has later been extended by C26 to derive different quantities (such as X-ray emissivity, Ly-α production rate, and ionizing photon production rate) that are critical for obtaining the 21-cm signal. Following C26, the effect of the astrophysically produced, i.e., "normal" AGN, is ignored in this work. It follows from the fact that these "normal" AGNs start to affect the 21-cm signal around $z \sim 5$ (Dayal et al. 2025), whereas the amplitude of the 21-cm signal (both global and power spectra) approaches zero by this redshift.

Here we briefly describe the important features of this framework, emphasising the calculation of key quantities related to the 21-cm signal.

1. In this model, the PBH seeds, forming at $z \sim 3400$, initially grow by linear accretion of dark matter around themselves until $z \sim 34$. After that, the halo growth becomes non-linear and finally begins to accrete gas once its baryonic overdensity reaches 200, triggering the star formation. At this point, the model accounts for feedback from both black hole accretion and star formation to calculate the subsequent evolution of the system until $z \sim 5$.
2. The bolometric luminosity of such an individual system at a redshift z is computed as

$$L_{\rm bol} = \epsilon_r \frac{\Delta M_{\rm PBH}\, c^2}{\Delta t}, \tag{4}$$

$\Delta M_{\rm PBH}$ is the mass accreted by the PBH seed after each time step of $\Delta t = 20$ Myr (Dayal 2024). Assuming the black holes to be non-spinning, the radiative efficiency ϵ_r is fixed at 0.057 to match existing astrophysical and cosmological constraints. [1]
3. From a given $L_{\rm bol}$, the X-ray luminosity, $L_{\rm X}$, has been obtained using the bolometric correction factor $k_{\rm X}$, defined as $k_{\rm X} = L_{\rm bol}/L_{\rm X}$. Following Duras et al. (2020), k_X is computed from the fitting function $k_{\rm X} = a\left[1 + \left(\frac{\log_{10}(L_{\rm bol}/L_\odot)}{b}\right)^c\right]$, with the best fit values of the free parameters given by $a = 10.96$, $b = 11.93$, $c = 17.79$. Once we calculate $L_{\rm X}$ of the individual system, the global X-ray emissivity is obtained using

$$\langle \epsilon_X^{\rm PBH} \rangle = \int \frac{dN}{dM_{\rm PBH}} \cdot L_X^{\rm PBH}\, dM_{\rm PBH} \tag{5}$$

4. The globally averaged Ly$-\alpha$ photon production rate by these systems at a redshift z is given by:

$$\langle \dot{n}_\alpha^{PBH} \rangle = \int \frac{dN}{dM_{PBH}} \frac{L_\alpha}{h_p \nu_\alpha} dM_{PBH}, \tag{6}$$

where, L_α is the Ly$-\alpha$ luminosity of each AGN obtained from the B-band luminosity, L_B assuming a power law index of -0.57 (Lusso et al. 2015). Further, L_B is calculated from $L_{\rm bol}$ using the fitting function from Marconi et al. (2004). A similar approach has been taken for calculating the number of ionizing photons from these PBH-seeded AGNs except with a power law index of -1.57 (Telfer et al. 2002).

In Fig-1, we show the mass functions obtained for three different PBH models, at $z \sim 5$, using the aforementioned analytical calculation. [2] We start by noting that the log-normal

[1] Note that, the remaining free parameters in the PHANES framework related to AGN and stellar feedback are adopted from Table-1 of Dayal & Maiolino (2026), corresponding to the non-spinning black hole scenario.

[2] Note that all the mass functions plotted here are normalized to a value of $10^{-5.27}$ cMpc^{-3} at z$\sim$ 10 for a PBH seed with mass $10^{4.65} M_\odot$.

(in magenta) and critical (in blue) mass functions show their peaks around $M_{\rm BH} \sim 10^5 M_\odot$, whereas their values are negliglbe in both higher ($M_{\rm BH} > 10^7 M_\odot$) and lower ($M_{\rm BH} < 10^3 M_\odot$) mass regime. This is expected from their functional forms given in eqn 1 and 3. We show that although the power-law model (in green) is dominated by the contribution from the lower mass black holes, it has a non-negligible contribution even from higher mass bins. As a sanity check, we show that each of these three mass functions is 2-3 orders of magnitude lower than that of the mass functions observed by JWST (Matthee et al. 2024; Taylor et al. 2025). This is only to be expected since we do not consider the contribution coming from astrophysically produced AGNs while computing the mass functions.

3. Simulation setup with SCRIPT

Next, we briefly describe the simulation setup employed in this study. We utilise an explicitly photon-conserving semi-numerical reionization model, SCRIPT, and extend its framework to incorporate the essential physics of the cosmic dawn. The baseline model was introduced in Choudhury & Paranjape (2018) and subsequently enhanced with key reionization processes, including inhomogeneous recombination and radiative feedback, as presented in Maity & Choudhury (2022a).

The model self-consistently predicts the thermal and ionization state of the Universe within a cosmologically representative simulation volume. It takes as input the density field (Δ_i, where i labels individual cells in the simulation grid) and the collapsed mass fraction ($f_{{\rm coll},i}$). These quantities are used to compute the effective number of ionizing photons through an astrophysical parameterisation of the ionizing efficiency, ζ. The product $\zeta f_{{\rm coll},i}$ represents the number of ionizing photons per baryon in each cell. These photons are then distributed across the source cell and its neighbouring cells to determine the ionization fraction, while explicitly enforcing photon conservation.

This effective photon budget is updated self-consistently in each cell to account for inhomogeneous recombination and radiative feedback. The recombination rate is computed by tracking the joint evolution of the ionization and density fields with redshift. To incorporate the impact of small-scale clustering of photon sinks, we adopt a globally averaged clumping factor ($C_{\rm HII} = 3$), consistent with results from hydrodynamical simulations (e.g. D'Aloisio et al. 2020). The recombination rates further depend on the thermal history of the gas, as discussed in Section 4. Photoionization heating is modelled by parameterising the temperature increase ($T_{\rm re}$) when a region transitions from neutral to ionized (Hui & Gnedin 1997; Furlanetto & Oh 2009; Keating et al. 2018; Maity & Choudhury 2022a,b).

Radiative feedback is incorporated by modifying the minimum halo mass threshold ($M_{{\rm min},i}$) for star formation. In neutral regions, this threshold is set by the atomic cooling limit. In contrast, in ionized regions it is determined by the Jeans mass at the virial overdensity ($M_{{\rm J},i}$). As the Jeans mass depends on the local temperature ($M_{{\rm J},i} \propto T_i^{3/2}$), our self-consistent treatment of thermal evolution allows us to dynamically update $M_{{\rm min},i}$, and consequently $f_{{\rm coll},i}$, thereby capturing the effects of radiative feedback.

As our focus is on large-scale observables, we generate the density field using second-order Lagrangian perturbation theory (2LPT) (Hahn & Abel 2011), rather than computationally expensive N-body simulations. The collapsed mass fraction is then estimated using a semi-analytic model based on conditional ellipsoidal collapse (Sheth & Tormen 2002). For this work, we adopt a simulation volume of size $L = 256\ h^{-1}$cMpc with a spatial resolution of $\Delta x = 8\ h^{-1}$cMpc. This box size is sufficient to capture the scales relevant for 21 cm observables (Iliev et al. 2014; Kaur et al. 2020). To model the evolution of the IGM during cosmic dawn and reionization, we generate 251 coeval simulation boxes spanning the redshift range $z = 5$–30, with a resolution of $\Delta z = 0.1$.

Below, we discuss the essential model components and their astrophysical significance. This further provides a physical background for the inclusion of the PBH contribution in the existing model setup.

1. The number of escaping ionizing photons produced per unit time at a redshift z is computed using

$$\dot{n}_{\rm ion,i} = \frac{dN_{\rm ion}}{dM} \times \rho_{\rm SFR,i} = \bar{\rho}_b \left(\frac{dN_{\rm ion}}{dM}\right) \frac{d}{dt} \langle f_* f_{\rm esc} f_{{\rm coll},i} \Delta_i \rangle \quad (7)$$

where, f_* is the star formation efficiency, $f_{\rm esc}$ is the escape fraction, and $\bar{\rho}_b$ is the mean comoving baryon density. Finally, $\frac{dN_{\rm ion}}{dM}$ is the number of ionizing photons produced per unit stellar mass.
Following the formalism developed in Maity & Choudhury (2022a), and defining $\zeta = 1.22 f_* f_{\rm esc} N_\gamma$, we can rewrite the above equation as

$$\dot{n}_{\rm ion,i} = \frac{\bar{n}_b}{1.22} \frac{d\langle \zeta f_{{\rm coll},i} \Delta_i \rangle}{dt} = \bar{n}_H \frac{d\langle \zeta f_{{\rm coll},i} \Delta_i \rangle}{dt} \quad (8)$$

where N_γ is the number of ionizing photons per unit baryons, $\bar{n}_b$ ($\bar{n}_H$) is the average baryon (hydrogen) number density. We adopt $N_\gamma = 4845$, motivated by typical values from Starburst99 (Leitherer et al. 1999) assuming a standard Salpeter IMF in the mass range $1-100\ M_\odot$ with a metallicity of $0.05 M_\odot$. We further assume a redshift-dependent star formation efficiency, $f_*(z) = f_{*,0} \left(\frac{10}{1+z}\right)^{\alpha_z}$. For the fiducial model, we assume $f_{*,0} = 0.005$, $\alpha_z = 4$, and fix the value of ionizing escape fraction $f_{\rm esc} = 0.12$ (Maity & Choudhury 2022b), ensuring the model matches with the existing constraints on reionization history (reionization start at $z \sim 10$ and ends at $z \sim 5.7$) as shown in the Appendix-A.1. As we aim to study the effect of PBH during cosmic dawn, a relatively sharp reionization history has been assumed to keep the cosmic dawn unaffected by the photoionization heating.
2. Following a similar definition, the Ly-α photon production rate at a redshift z in the i^{th} cell is given by

$$\dot{n}^{\rm SF}_{\alpha,i} = \bar{\rho}_b \left(\frac{dN_\alpha}{dM}\right) \frac{d\langle f_* f_{\rm esc} f_{{\rm coll},i} \Delta_i \rangle}{dt} = \bar{n}_b N_{\gamma,\alpha} \frac{d\langle f_* f_{\rm esc} f_{{\rm coll},i} \Delta_i \rangle}{dt} \quad (9)$$

where $N_{\gamma,\alpha}$ is the number of Ly-α photons per unit baryon, which is assumed to be twice that of ionizing photons, i.e., 9690. We further add 4800, taking into account the Pop-III stellar contribution (Furlanetto et al. 2006).
3. The evolution of the global ionization fraction ($Q_{\rm HII}$) can be written as

$$\frac{dQ_{\rm HII,i}}{dt} = \frac{d\langle \zeta f_{{\rm coll},i} \Delta_i \rangle}{dt} - Q_{\rm HII,i} \alpha_A C_{\rm HII} \chi_{He} \bar{n}_H (1+z)^3 \quad (10)$$

where χ_{He} is the correction factor on electron number density due to Helium ionization, $C_{\rm HII}$ is the clumping factor of the IGM (fixed at 3), and α_A is the (case A) recombination rate coefficient. Note that we do not consider the contribution of PBHs while calculating the ionization history as the ionizing photons coming from different PBH models are completely negligible compared to SF galaxies (discussed later in Sec-5).

4. The 21-cm signal

The 21-cm differential brightness temperature can be written as (Pritchard & Loeb 2012; Mena et al. 2019)

$$\delta T_{b,i} \simeq 27\,{\rm mK}\;\; x_{{\rm HI},i}\Delta_i \left(\frac{\Omega_b h^2}{0.023}\right)\left(\frac{1+z}{10}\frac{0.15}{\Omega_m H^2}\right)^{1/2}\left(1-\frac{T_{\gamma,i}}{T_{S,i}}\right) \quad (11)$$

where $x_{{\rm HI},i}$ denotes the neutral hydrogen fraction of the IGM, $T_{\gamma,i}(z)$ is the background CMB temperature given by $T_{\gamma,i} \equiv T_\gamma = 2.73\,(1+z)$ K. Finally, $T_{S,i}$, the spin temperature of the Hydrogen atom, can be written as

$$T_{S,i}^{-1} = \frac{T_\gamma^{-1} + x_{\alpha,i}T_{K,i}^{-1} + x_{c,i}T_{K,i}^{-1}}{1 + x_{c,i} + x_{\alpha,i}} \quad (12)$$

where x_α is the Ly-α coupling coefficients, x_c is the collisional coupling coefficient and $T_{K,i}$ is the kinetic temperature of the IGM.

Another observable of our interest for this study is the dimensionless 21 cm power spectrum, defined as

$$\Delta_{21}^2 = \frac{k^3 P_{21}(k)}{2\pi^2} \quad (13)$$

where $P_{21}(k)$ is the power spectrum of the mean-subtracted fluctuation field $\delta T_{b,i} - \langle \delta T_{b,i}\rangle$.

The collisional coupling coefficient, $x_{c,i}$ is determined using the standard fitting functions described in Pritchard & Loeb (2012), whereas all the other terms appearing in eqn 12 have been described as follows.

4.1. Kinetic temperature of the IGM

The temperature evolution of the IGM can be expressed as

$$\frac{dT_{k,i}}{dz} = \frac{2T_{k,i}}{1+z} + \frac{dt}{dz}\frac{2}{3}\frac{\epsilon_i}{k_B n_{{\rm tot},i}} \quad (14)$$

where the first term on the right-hand side denotes the adiabatic cooling due to the expansion of the Universe, and the second term represents the net heating rate per unit volume for the $i^{\rm th}$ cell from different astrophysical processes. While we follow Furlanetto et al. (2006) for computing the adiabatic cooling, here we explain in detail the calculation of the second term.

The net heating rate can be expanded as (Furlanetto et al. 2006; Maity & Choudhury 2022a)

$$\frac{2}{3}\frac{\epsilon_i}{k_B n_{{\rm tot},i}} = \frac{2}{3}\frac{1}{k_B n_{{\rm tot},i}}\left(\epsilon_{X,i}^{\rm SF+PBH} + \epsilon_{{\rm re},i}^{\rm SF} + \epsilon_{{\rm comp},i}\right) \quad (15)$$

where the first term denotes the total X-ray heating of the IGM coming due to both SF and PBH-seeded galaxies. Further, $\epsilon_{{\rm re},i}$ represents the heating due to reionization, and finally $\epsilon_{{\rm comp},i}$ indicate Compton cooling. We follow Maity & Choudhury (2022a) in order to determine $\epsilon_{{\rm re},i}$, and $\epsilon_{{\rm comp},i}$. Specifically, $\epsilon_{{\rm re},i}$ is essentially proportional to the reionization temperature increment ($T_{\rm re}$) parameter, which has been mentioned in Section 3. Finally, combining the contribution of the SF and PBH galaxies, the total X-ray heating term, i.e., $\epsilon_{X,i}^{\rm SF+PBH}$, can be written as

$$\epsilon_{X,i}^{\rm SF+PBH} = f_h\left[f_{X,{\rm esc}}^{\rm SF}\epsilon_X^{\rm SF} + f_{X,{\rm esc}}^{\rm PBH}\epsilon_X^{\rm PBH}\right] \quad (16)$$

where f_h is the fraction of X-ray that heats the IGM and is taken to be $\sim \left(1 + \frac{2x_{{\rm HII},i}}{3}\right)$, with $x_{{\rm HII},i}$ being the ionization fraction (Furlanetto et al. 2006). Further, $f_{X,{\rm esc}}^{\rm SF}$ and $f_{X,{\rm esc}}^{\rm PBH}$ are the fraction of X-ray escaping the host galaxies for SF and PBH seeded systems. [3] Next, we describe each component of this term.

X-ray from SF: Assuming that the relation between X-ray luminosity and the star formation rate density ($\rho_{\rm SFR}$) in the local Universe holds also in the high-z Universe, the X-ray emissivity can be expressed as (Mineo et al. 2012; Furlanetto et al. 2006)

$$\frac{2\epsilon_{X,i}^{\rm SF}}{3k_B n_{{\rm tot},i} H(z)} = 5\times 10^3\; K\left(\frac{f_*}{0.1}\frac{{\rm d}f_{\rm coll}/{\rm d}z}{0.01}\frac{1+z}{10}\right) \quad (17)$$

X-ray from PBH: For PBH, the X-ray emissivity in the $i^{\rm th}$ cell is given by

$$\epsilon_{X,i}^{\rm PBH} = \Delta_i\langle\epsilon_X^{\rm PBH}\rangle \quad (18)$$

where we assume that the X-ray emissivity in the $i^{\rm th}$ cell can be obtained by multiplying the global X-ray emissivity $\langle\epsilon_X^{\rm PBH}\rangle$ (from eqn 5) by the overdensity of the $i^{\rm th}$ cell.

4.2. Ly-α coupling

The Ly-α coupling coefficient $x_{\alpha,i}$ is defined as

$$x_{\alpha,i} = 1.81\times 10^{11}\,(1+z)^{-1} S_\alpha \frac{J_{\alpha,i}}{\rm cm^{-2}sec^{-1}Hz^{-1}sr^{-1}} \quad (19)$$

where $J_{\alpha,i}$ is the Ly-α background flux. S_α is a factor coming from a detailed analysis of atomic physics, and following the general practice, we take it to be unity (Furlanetto et al. 2006).

Finally, including the effect of both SF and PBH-seeded galaxies, the background Ly-α flux can be written as (Mena et al. 2019)

$$J_{\alpha,i}^{\rm SF+PBH} = \frac{c}{4\pi}\frac{1}{H(z)\nu_\alpha}\left[f_\alpha^{\rm SF}\dot{n}_{\alpha,i}^{\rm SF}(z) + f_\alpha^{\rm PBH}\dot{n}_{\alpha,i}^{\rm PBH}(z)\right] \quad (20)$$

with $\dot{n}_{\alpha,i}^{\rm SF}(z)$ given by eqn 9 and $\dot{n}_{\alpha,i}^{\rm PBH} = \Delta_i\langle\dot{n}_\alpha^{\rm PBH}\rangle$. Further, $f_\alpha^{\rm SF}$ and $f_\alpha^{\rm PBH}$ are the escaping fraction of the Ly-α photons from SF and PBH-seeded galaxies. For the sake of simplicity, we assume both of them to be 1.

[3] We also note that these factors will absorb any uncertainty that may come from using the low-redshift $\epsilon_X - \rho_{\rm SFR}$ calibration relation while determining the X-ray contribution from SF and PBH galaxies.

5. Effect of PBHs on 21-cm signal

We begin by describing Fig. 2, which illustrates the redshift evolution of the quantities critical for the determination of the 21-cm signal. In all panels, the magenta, green, and blue curves correspond to the lognormal, power-law, and critical PBH mass functions, respectively, while the black curve represents the contribution from star-forming (SF) galaxies (for a fiducial scenario).

In the left-most panel, we show the redshift evolution of the X-ray emissivity for different models studied in this work. First, we note that all PBH models produce significantly higher X-ray emission than SF galaxies at $z \geq 15$, reflecting the earlier onset of X-ray production in PBH-seeded systems compared to SF galaxies. In the range $10 \leq z < 15$, the critical mass function produces the highest X-ray emissivity, followed by the power-law model and SF galaxies, while the lognormal PBH model yields the lowest emission. Keeping in mind that the emission from individual galaxies is independent of the specific mass function, this behaviour can be qualitatively understood from the overall shapes of the mass functions of different PBH models shown in Fig. 1. The critical mass function, with its highest peak, yields the strongest emission. Although the lognormal mass function attains a higher peak than the power-law form, the latter's extended tail results in a greater overall contribution, ultimately surpassing the lognormal mass function. Finally, at $z \lesssim 8$, the X-ray emission from power-law PBHs exceeds that of the critical mass function. This is attributed to the extended high-mass tail of the power-law distribution, whereas the critical mass function is sharply peaked and contributes negligibly at higher masses.

The centre and right-most panels show the redshift evolution of the background Ly-α flux (J_α) and the ionizing photon production rate ($\dot{n}_{\rm ion}$), respectively. Since both Ly-α and ionizing photons are produced predominantly via star formation, it is expected that SF galaxies generate Ly-α and ionizing photons several orders of magnitude higher than any of the PBH models over the entire redshift range. Further, among different PBH models, the critical mass function yields the most, followed by the powerlaw mass function, whereas the lognormal PBH model produces the lowest emission. Similar to the explanation of the X-ray emission in the left-most panel, this can again be attributed to the shape and normalisation of different mass functions, as shown in Fig. 1.

Now, we move to our main result depicted in Fig-3. The left panel shows the redshift evolution of the global 21-cm signal corresponding to different models, whereas the right panel shows the observable for the 21-cm power spectrum, $\langle \delta T_b \rangle^2 \Delta^2_{21}$ computed at $k \sim 0.1\,h\,{\rm cMpc}^{-1}$ in the entire redshift range of our interest. Before going into the detailed discussion, we would like to remind the reader that for all these models depicted in this figure, $f^{\rm SF}_\alpha = f^{\rm PBH}_\alpha = f^{\rm SF}_{X,\rm esc} = f^{\rm PBH}_{X,\rm esc} = 1.0$.

For the global signal, the lognormal (in magenta) and power law PBHs (in green) produce similar redshift evolution with absorption trough of ~ -30 at a redshift of $z \sim 18$, whereas the 21-cm global signal coming from the PBHs following critical mass functions (in blue) is very distinct compared to both of these models. In fact, it does not even produce any absorption trough. This behaviour can be explained from a closer inspection of the X-ray emissivity produced from different models shown in the left-most panel of Fig-2. In Fig-2, we find that the X-ray emissivity is highest for critical and lowest for the lognormal, with powerlaw model in between them. Keeping in mind that the depth of the signal is effectively determined by the X-ray heating in the IGM for these systems (as the Ly-α background is very similar for all the PBH models), the model with the maximum X-ray heating (i.e., critical mass function) will produce the shallowest trough, and the model with the lowest X-ray emission (i.e., lognormal mass function) will produce the deepest trough. Finally, we also show the 21-cm signal produced from an SF-only model (in black) with no contribution from PBH-seeded systems. As expected, the SF-only model shows the deepest absorption trough of ~ -60 mK without any X-ray heating coming from PBH-seeded systems. The finding that models with PBH contribution will show a shallower absorption trough compared to models without PBH contribution has also been found in C26.

The power spectra (the right panel of Fig-3) contain three distinct peaks corresponding to Ly-α coupling, X-ray heating, and reionization heating, respectively, at higher to lower redshifts. It is apparent that the PBH heating suppresses the amplitude of the power spectra during the cosmic dawn. Specifically, the powerlaw and lognormal cases show more than a factor of half reduction on the power amplitude ($\sim 20 - 30\ mK^2$ from the SF-only case ($\sim 100\ mK^2$). This effect is more striking for the critical case, where a suppression of more than a couple of orders of magnitude can be seen. However, all the scenarios are still allowed by the existing limits from the recent interferometric observations. The qualitative effects are consistent with the previous studies (Mena et al. 2019). We note that PBHs do not affect the power-spectrum amplitude during the reionization epoch, as they do not contribute to ionization in our model. However, these effects can be highly degenerate with the photoionization heating if the reionization is extended to cosmic dawn (unlike our fiducial case).

Another important aspect of this work is to examine the impact of varying $f^{\rm PBH}_{X,\rm esc}$, the fraction of X-ray photons escaping the host galaxies, for the lognormal PBH model on the 21-cm signal. This is crucial as this parameter is highly uncertain from both observational and theoretical perspectives. In fact, the recent JWST observations of these early AGNs (Maiolino et al. 2025; Yue et al. 2024; Ananna et al. 2024; Mazzolari et al. 2025) estimated a very weak X-ray emission compared to AGNs in the local Universe. In view of this, we varied $f^{\rm PBH}_{X,\rm esc}$ from 1.0 to 0.2 as shown in Fig. 4. The dashed magenta line corresponds to the lognormal model with $f^{\rm PBH}_{X,\rm esc} = 0.2$, while the solid magenta line represents the case with $f^{\rm PBH}_{X,\rm esc} = 1.0$. For comparison, the SF-only scenario is shown by the black curve. We note that the solid magenta and black curves are also presented in Fig. 3. As $f^{\rm PBH}_{X,\rm esc}$ is lowered from 1.0 to 0.2, the absorption trough becomes progressively deeper, approaching that of the SF-only model. This behaviour is expected, as a lower escape fraction results in reduced X-ray heating of the intergalactic medium, thereby enhancing the depth of the absorption feature. A similar impact can be noticed for the power spectra as in the previous ones. An increasing PBH heating efficiency results in suppression of power amplitude. Although an efficiency, $f^{\rm PBH}_{X,\rm esc} = 0.2$, produces a similar trend as the SF-only case, the effect of a higher efficiency ($f^{\rm PBH}_{X,\rm esc} = 1.0$) can be significant enough to be distinguishable by the upcoming interferometers. Since this qualitative trend is similar across all PBH models considered in this work, we restrict our discussion here to the lognormal case.

6. Conclusions and Discussion

In this work, we (*i*) apply the PBH analytical model `PHANES` to three physically motivated PBH mass functions, i.e., lognormal,

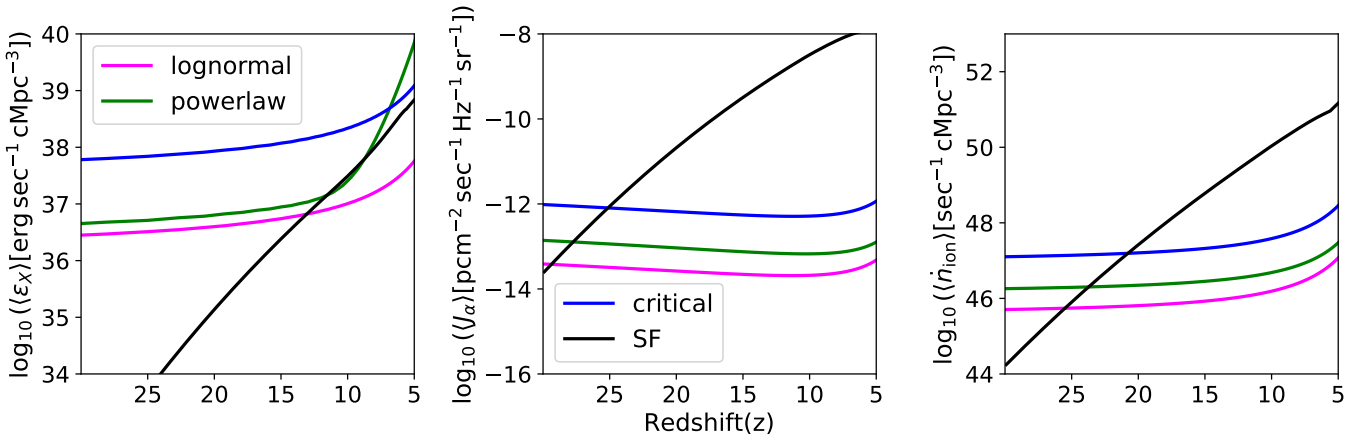

Fig. 2. Redshift evolution of the global X-ray emissivity, Ly-α background flux and Ionizing photon production rate for different PBH models along with the SF galaxies. The black, magenta, green, and blue lines respectively denote SF, lognormal, powerlaw and critical PBH seeded systems as mentioned in the legends.

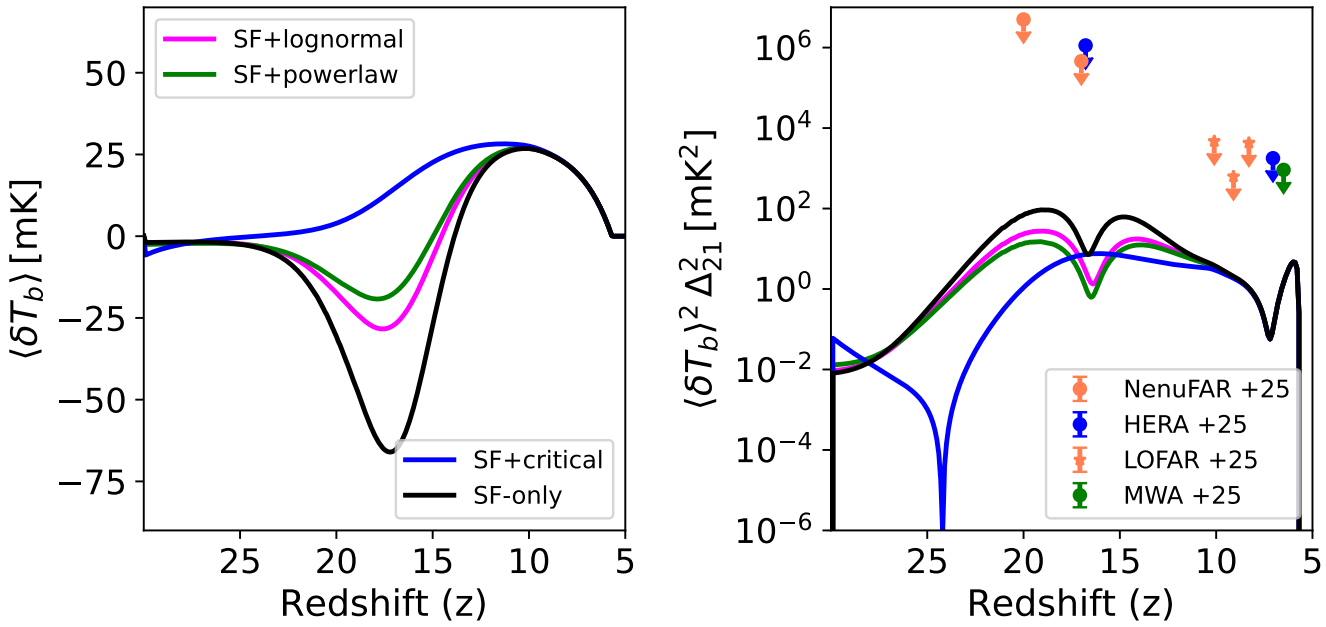

Fig. 3. The redshift evolution of the 21-cm global signal and the power spectrum (computed at $k \sim 0.1\,h\,\mathrm{cMpc}^{-1}$) corresponding to different models studied in this paper. The legends in the left panel show the colour scheme for various models, whereas the legends in the right panel show the upper limits obtained from different observations.

power-law, and critical to compute key quantities relevant to the 21-cm signal; and (*ii*) extend the explicitly photon-conserving reionization model SCRIPT to incorporate the essential physics of cosmic dawn, and finally (*iii*) couple the two frameworks to investigate the impact of different PBH mass functions on both the global 21-cm signal and its power spectrum over the redshift range $5 \leq z \leq 30$. Our main findings are as follows:

- The inclusion of early AGNs leads to a significant impact on both the global 21-cm signal and its power spectrum compared to models that include only SF galaxies. This trend is observed for all PBH mass functions considered in this study.
- The global signal and the 21-cm power spectrum corresponding to the critical mass function differ significantly from those obtained from lognormal and powerlaw mass functions.
- Finally, we examine the effect of varying the escape fraction of X-ray photons from PBH-seeded galaxies in the case of the lognormal mass function. We find that as this fraction decreases, the resulting X-ray heating is reduced, causing the signal to progressively approach the SF-only scenario in the limit of vanishing escape fraction.

We conclude by noting a few caveats of this study. Most importantly, we have not considered the contribution of radio emission from early AGNs. Such emission could, in principle, lead to a deeper absorption trough by counteracting the effect of enhanced X-ray heating (Ewall-Wice et al. 2020; Nelander et al. 2025). However, we do not include this effect,

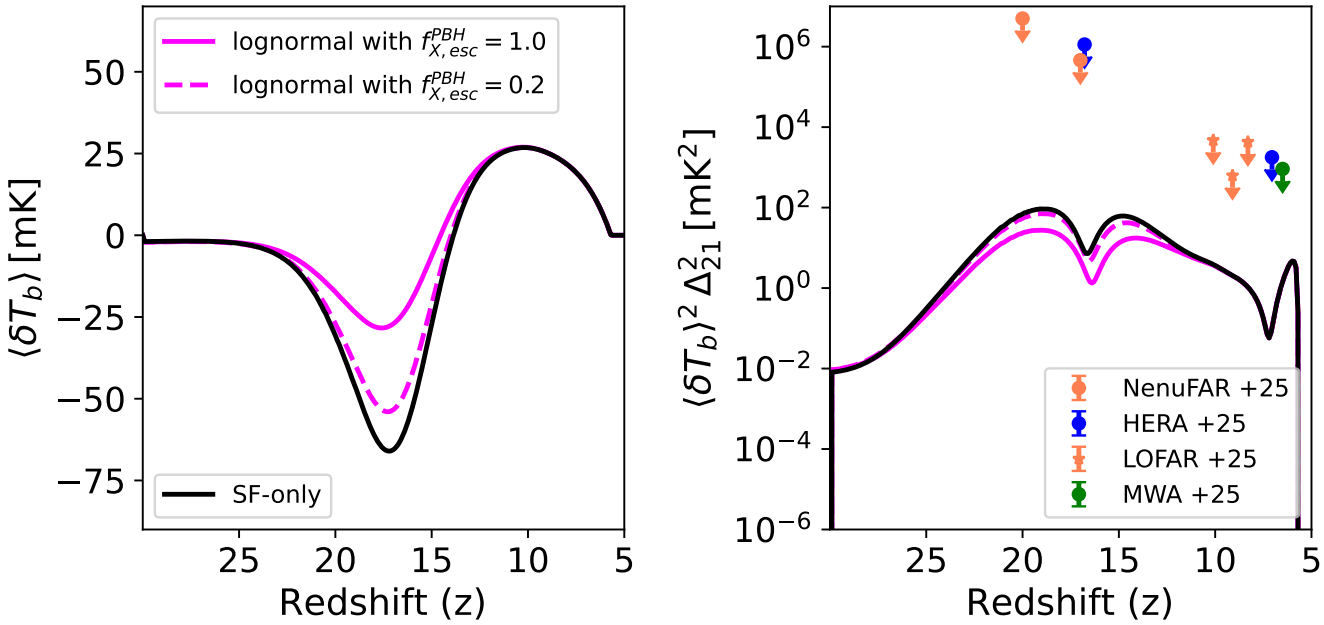

Fig. 4. Effect of varying $f_{X,\mathrm{esc}}^{\mathrm{PBH}}$ in the lognormal mass function. As mentioned in the legend, the dashed magenta line shows the scenario with $f_{X,\mathrm{esc}}^{\mathrm{PBH}} = 1.0$, whereas the solid magenta line represents the case with $f_{X,\mathrm{esc}}^{\mathrm{PBH}} = 1.0$. Further, the black line shows the SF-Only scenario.

as current observations suggest that these early AGNs produce very weak radio emission compared to AGNs observed in the local Universe (Mazzolari et al. 2025, 2026). We plan to include the radio emission in our future work. Secondly, we modelled the X-ray heating effects by assuming a simplistic semi-analytic form (Furlanetto et al. 2006), that may not be realistic on smaller scales. The model can be improved with more accurate small-scale physics in the future, although the large-scale features are unlikely to change significantly. Furthermore, this framework can also be incorporated with an explicit contribution from Pop-III stars and feedback from Lyman-Werner background (Ventura et al. 2023), which may play a crucial role in IGM evolution during the cosmic dawn. We note that the current study demonstrates the impact of PBH effects on a fiducial star-formation evolution model, which has significant space for variation, allowing present observational constraints (i.e., Appendix B shows the signal for a couple of other SF variants). We also checked the resolution dependencies of the relevant observables in the semi-numerical setup as a robustness measure (see Appendix C). We found that the qualitative conclusions remain the same, even though the different resolutions have slightly different quantitative estimates of the observable effects.

Acknowledgements. The work of AC was supported by the European Union's Horizon Europe research and innovation programme under the Marie Skłodowska-Curie Postdoctoral Fellowship HORIZON-MSCA-2023-PF-01, grant agreement No 101151693 (LUPCOS). AC acknowledges the use of CHATGPT for refining the text at the final stage of the manuscript.

References

Albrecht, A. & Steinhardt, P. J. 1982, Phys. Rev. Lett., 48, 1220
Ananna, T. T., Bogdán, Á., Kovács, O. E., Natarajan, P., & Hickox, R. C. 2024, ApJ, 969, L18
Barkana, R. & Loeb, A. 2001, Phys. Rep., 349, 125
Bogdán, Á., Goulding, A. D., Natarajan, P., et al. 2024, Nature Astronomy, 8, 126
Bosman, S. E. I., Davies, F. B., Becker, G. D., et al. 2022, MNRAS, 514, 55
Bowman, J. D., Rogers, A. E. E., Monsalve, R. A., Mozdzen, T. J., & Mahesh, N. 2018, Nature, 555, 67
Carr, B., Kohri, K., Sendouda, Y., & Yokoyama, J. 2021, Reports on Progress in Physics, 84, 116902
Carr, B., Kohri, K., Sendouda, Y., & Yokoyama, J. 2021, Rept. Prog. Phys., 84, 116902
Carr, B. & Kuhnel, F. 2020, Ann. Rev. Nucl. Part. Sci., 70, 355
Carr, B. & Kuhnel, F. 2025 [arXiv:2502.15279]
Carr, B., Raidal, M., Tenkanen, T., Vaskonen, V., & Veermäe, H. 2017, Phys. Rev. D, 96, 023514
Carr, B. J. 1975, Astrophys. J., 201, 1
Carr, B. J. & Green, A. M. 2024, arXiv e-prints, arXiv:2406.05736
Carr, B. J. & Hawking, S. W. 1974, Mon. Not. Roy. Astron. Soc., 168, 399
Carr, B. J., Kohri, K., Sendouda, Y., & Yokoyama, J. 2010, Phys. Rev. D, 81, 104019
Chatterjee, A. 2026, arXiv e-prints, arXiv:2601.10304
Chatterjee, A., Choudhury, T. R., & Mitra, S. 2021, MNRAS, 507, 2405
Chatterjee, A., Dayal, P., & Mauerhofer, V. 2023, MNRAS, 525, 620
Chen, L., Huang, Q.-G., & Wang, K. 2016, JCAP, 12, 044
Choptuik, M. W. 1993, Phys. Rev. Lett., 70, 9
Choudhury, T. R. & Paranjape, A. 2018, MNRAS, 481, 3821
Cumner, J., de Lera Acedo, E., de Villiers, D. I. L., et al. 2022, Journal of Astronomical Instrumentation, 11, 2250001
D'Aloisio, A., McQuinn, M., Trac, H., Cain, C., & Mesinger, A. 2020, ApJ, 898, 149
Davies, F. B., Hennawi, J. F., Bañados, E., et al. 2018, ApJ, 864, 142
Dayal, P. 2024, A&A, 690, A182
Dayal, P. & Maiolino, R. 2026, A&A, 706, A72
Dayal, P., Volonteri, M., Choudhury, T. R., et al. 2020, MNRAS, 495, 3065
Dayal, P., Volonteri, M., Greene, J. E., et al. 2025, A&A, 697, A211
DeBoer, D. R., Parsons, A. R., Aguirre, J. E., et al. 2017, PASP, 129, 045001
Dhandha, J., Fialkov, A., Gessey-Jones, T., et al. 2025, MNRAS, 542, 2292
Dienes, K. R., Heurtier, L., Huang, F., Tait, T. M. P., & Thomas, B. 2025, Phys. Rev. D, 112, 083547
Dolgov, A. & Silk, J. 1993, Phys. Rev. D, 47, 4244
Dolgov, A. & Silk, J. 1993, Phys. Rev. D, 47, 4244
Duras, F., Bongiorno, A., Ricci, F., et al. 2020, A&A, 636, A73
Ewall-Wice, A., Chang, T.-C., & Lazio, T. J. W. 2020, MNRAS, 492, 6086
Furlanetto, S. R. & Oh, S. P. 2009, ApJ, 701, 94
Furlanetto, S. R., Oh, S. P., & Briggs, F. H. 2006, Phys. Rep., 433, 181
Gessey-Jones, T., Sartorio, N. S., Bevins, H. T. J., et al. 2025, Nature Astronomy, 9, 1268
Ghara, R., Giri, S. K., Ciardi, B., Mellema, G., & Zaroubi, S. 2021, MNRAS, 503, 4551

Gillet, N., Mesinger, A., Greig, B., Liu, A., & Ucci, G. 2019, MNRAS, 484, 282
Gong, J.-O. & Kitajima, N. 2017, J. Cosmology Astropart. Phys., 2017, 017
Gouttenoire, Y., Trifinopoulos, S., Valogiannis, G., & Vanvlasselaer, M. 2024, Phys. Rev. D, 109, 123002
Greene, J. E., Labbe, I., Goulding, A. D., et al. 2024, ApJ, 964, 39
Greig, B. & Mesinger, A. 2015, MNRAS, 449, 4246
Greig, B. & Mesinger, A. 2018, MNRAS, 477, 3217
Greig, B., Mesinger, A., Davies, F. B., et al. 2022, MNRAS, 512, 5390
Gundlach, C. 1997, Phys. Rev. D, 55, 695
Hahn, O. & Abel, T. 2011, MNRAS, 415, 2101
Hawking, S. 1971, Mon. Not. Roy. Astron. Soc., 152, 75
HERA Collaboration, Abdurashidova, Z., Adams, T., et al. 2023, ApJ, 945, 124
Hui, L. & Gnedin, N. Y. 1997, MNRAS, 292, 27
Hutter, A., Dayal, P., Yepes, G., et al. 2021, MNRAS, 503, 3698
Iliev, I. T., Mellema, G., Ahn, K., et al. 2014, MNRAS, 439, 725
Jin, X., Yang, J., Fan, X., et al. 2023, ApJ, 942, 59
Kaur, H. D., Gillet, N., & Mesinger, A. 2020, MNRAS, 495, 2354
Keating, L. C., Puchwein, E., & Haehnelt, M. G. 2018, MNRAS, 477, 5501
Kern, N. S., Liu, A., Parsons, A. R., Mesinger, A., & Greig, B. 2017, ApJ, 848, 23
Kohri, K., Sekiguchi, T., & Wang, S. 2022, Phys. Rev. D, 106, 043539
Koushiki, Goswami, R., & Joshi, P. S. 2025a [arXiv:2512.20998]
Koushiki, Joshi, P. S., & Bhattacharyya, S. 2025b [arXiv:2501.14695]
Kovács, O. E., Bogdán, Á., Natarajan, P., et al. 2024, ApJ, 965, L21
Krasnov, M. A. & Nikulin, V. V. 2023, Particles, 6, 580
Leitherer, C., Schaerer, D., Goldader, J. D., et al. 1999, ApJS, 123, 3
Linde, A. 1983, Physics Letters B, 129, 177
Liu, B. & Bromm, V. 2022, ApJ, 937, L30
Liu, B. & Bromm, V. 2023, arXiv e-prints, arXiv:2312.04085
Lucchin, F. & Matarrese, S. 1985, Phys. Rev. D, 32, 1316
Lusso, E., Worseck, G., Hennawi, J. F., et al. 2015, MNRAS, 449, 4204
Maiolino, R., Risaliti, G., Signorini, M., et al. 2025, MNRAS, 538, 1921
Maity, B. & Choudhury, T. R. 2022a, MNRAS, 511, 2239
Maity, B. & Choudhury, T. R. 2022b, MNRAS, 515, 617
Marconi, A., Risaliti, G., Gilli, R., et al. 2004, MNRAS, 351, 169
Matteri, Antonio, Ferrara, Andrea, & Pallottini, Andrea. 2025, A&A, 701, A186
Matthee, J., Naidu, R. P., Brammer, G., et al. 2024, ApJ, 963, 129
Mazzolari, G., Gilli, R., Maiolino, R., et al. 2026, A&A, 706, A372
Mazzolari, G., Scholtz, J., Maiolino, R., et al. 2025, A&A, 700, A12
Mena, O., Palomares-Ruiz, S., Villanueva-Domingo, P., & Witte, S. J. 2019, Phys. Rev. D, 100, 043540
Mertens, F. G., Mevius, M., Koopmans, L. V. E., et al. 2025, A&A, 698, A186
Mesinger, A., ed. 2019, The Cosmic 21-cm Revolution, 2514-3433 (IOP Publishing)
Mineo, S., Gilfanov, M., & Sunyaev, R. 2012, Monthly Notices of the Royal Astronomical Society, 419, 2095
Mittal, S., Ray, A., Kulkarni, G., & Dasgupta, B. 2022, J. Cosmology Astropart. Phys., 2022, 030
Mosani, K., Koushiki, Joshi, P. S., Trivedi, J. V., & Bhanja, T. 2023, Phys. Rev. D, 108, 044049
Munshi, S., Mertens, F. G., Koopmans, L. V. E., et al. 2024, A&A, 681, A62
Musco, I., Jedamzik, K., & Young, S. 2024, Phys. Rev. D, 109, 083506
Musco, I. & Miller, J. C. 2013, Classical and Quantum Gravity, 30, 145009
Napolitano, L., Castellano, M., Pentericci, L., et al. 2025, A&A, 693, A50
Napolitano, L., Castellano, M., Pentericci, L., et al. 2024, arXiv e-prints, arXiv:2410.18763
Nelander, A., Cain, C., DSilva, J. C. J., et al. 2025, arXiv e-prints, arXiv:2507.21230
Nhan, B. D., Bordenave, D. D., Bradley, R. F., et al. 2018, arXiv e-prints, arXiv:1811.04917
Nunhokee, C. D., Null, D., Trott, C. M., et al. 2025, ApJ, 989, 57
Onoue, M., Kashikawa, N., Willott, C. J., et al. 2017, ApJ, 847, L15
Paciga, G., Albert, J. G., Bandura, K., et al. 2013, MNRAS, 433, 639
Planck Collaboration, Ade, P. A. R., Aghanim, N., et al. 2016, A&A, 594, A13
Pritchard, J. R. & Loeb, A. 2012, Reports on Progress in Physics, 75, 086901
Pritchard, J. R. & Loeb, A. 2012, Reports on Progress in Physics, 75, 086901
Saha, A. K. & Laha, R. 2022, Phys. Rev. D, 105, 103026
Schneider, R., Valiante, R., Trinca, A., et al. 2023, MNRAS, 526, 3250
Sheth, R. K. & Tormen, G. 2002, Monthly Notices of the Royal Astronomical Society, 329, 61
Sims, P. H., Bevins, H. T. J., Fialkov, A., et al. 2025, MNRAS[arXiv:2504.09725]
Singh, S., Jishnu, N. T., Subrahmanyan, R., et al. 2022, Nature Astronomy, 6, 607
Sokolowski, M., Tremblay, S. E., Wayth, R. B., et al. 2015, PASA, 32, e004
Spina, B., Bosman, S. E. I., Davies, F. B., Gaikwad, P., & Zhu, Y. 2024, A&A, 688, L26
Tashiro, H. & Sugiyama, N. 2013, MNRAS, 435, 3001
Taylor, A. J., Kokorev, V., Kocevski, D. D., et al. 2025, arXiv e-prints, arXiv:2505.04609
Telfer, R. C., Zheng, W., Kriss, G. A., & Davidsen, A. F. 2002, ApJ, 565, 773
Tingay, S. J., Goeke, R., Bowman, J. D., et al. 2013, PASA, 30, e007
Trebitsch, M., Hutter, A., Dayal, P., et al. 2023a, MNRAS, 518, 3576
Trebitsch, M., Hutter, A., Dayal, P., et al. 2023b, MNRAS, 518, 3576
van Haarlem, M. P., Wise, M. W., Gunst, A. W., et al. 2013, A&A, 556, A2
Ventura, E. M., Trinca, A., Schneider, R., et al. 2023, MNRAS, 520, 3609
Voytek, T. C., Natarajan, A., Jáuregui García, J. M., Peterson, J. B., & López-Cruz, O. 2014, ApJ, 782, L9
Yang, Y. 2021, Phys. Rev. D, 104, 063528
Yokoyama, J. 1998, Phys. Rev. D, 58, 107502
Yuan, G.-W., Lei, L., Wang, Y.-Z., et al. 2024, Science China Physics, Mechanics, and Astronomy, 67, 109512
Yue, M., Eilers, A.-C., Ananna, T. T., et al. 2024, ApJ, 974, L26
Zhao, M.-L., Shao, Y., Wang, S., & Zhang, X. 2026, Chinese Physics C, 50, 025101
Zhao, M.-L., Wang, S., & Zhang, X. 2025, J. Cosmology Astropart. Phys., 2025, 039
Zhu, Y., Becker, G. D., Bosman, S. E. I., et al. 2024, MNRAS, 533, L49
Ziparo, F., Gallerani, S., & Ferrara, A. 2025, J. Cosmology Astropart. Phys., 2025, 040

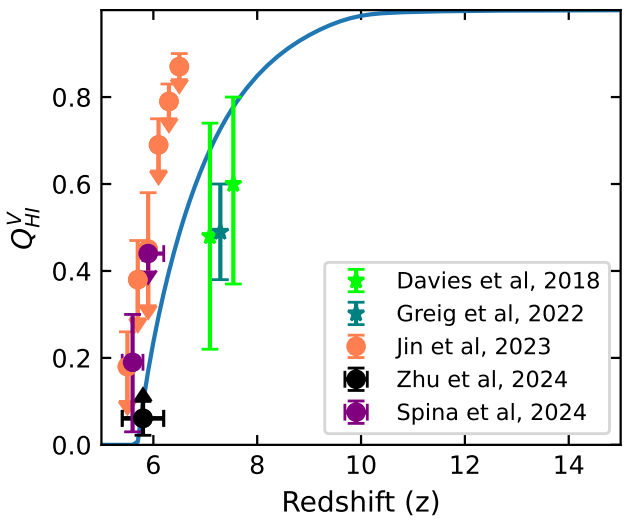

Fig. A.1. The fiducial ionization history (a fast evolving case with $f_* \propto (1+z)^{-4}$, obeying existing constraints on the IGM neutral fraction.

Appendix A: Fiducial reionization model

In Figure A.1, we showed the reionization history of our fiducial model, assumed in this study. We chose a fast reionization evolution with $f_* = 0.005\left(\frac{10}{1+z}\right)^4$, keeping the cosmic dawn window unaffected from photoionization heating. However, the model obeys different existing constraints on the ionization histories, mainly coming from the Ly-α forest (Jin et al. 2023; Zhu et al. 2024; Spina et al. 2024) and the damping wing analysis (Davies et al. 2018; Greig et al. 2022) of the high redshift quasar spectra. The model also follows a late reionization end, which is in accord with the recently emerging scenario (Bosman et al. 2022).

Appendix B: Effect of varying $f_{*,0}$ on the 21-cm signal

We have shown in Fig B.1, 21-cm signal (the global as well as the power spectra) with varying the $f_{*,0}$. This exercise has been performed to check whether the newly extended SCRIPT framework is implemented correctly. The left panel shows the global signal. As can be seen, with higher value of $f_{*,0}$, the absorption trough appears at earlier redshift. For example, with $f_{*,0} = 0.05$, the trough appears at $z \sim 20$, whereas for $f_{*,0} = 0.005$, the absorption trough appears at $z \sim 18$. Further models with increasing $f_{*,0}$ also reaches zero at earlier redshift since reionization is completed earlier in those models. Similar effect has also been observed for the power spectrum, shown in the right panel of Fig B.1. Here, all the peaks (related to Ly-α, X-ray heating and reionization), has shifted to earlier redshift as we increase the value of $f_{*,0}$.

Appendix C: Comparison between resolutions

In Fig C.1, we show the comparison of global 21 cm signal along with power spectra, for two different resolutions of the box (i.e., fiducial with $\Delta x = 8h^{-1}$cMpc and a higher resolution variant with $\Delta x = 4h^{-1}$cMpc). We note that the differences are maximum near the trough and agree well with each other for most of the redshifts. In both the cases, we Assumed $f_{*,0} = 0.005$ and $f_{X,\rm esc}^{\rm SF} = 1.0$.

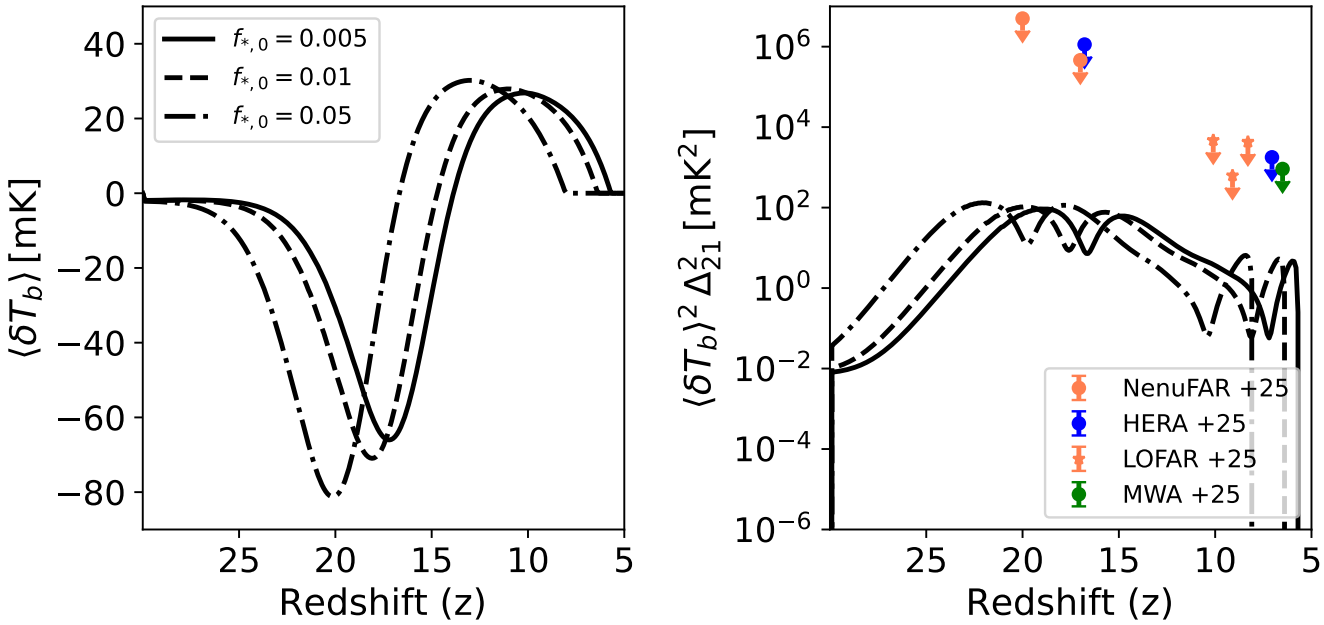

Fig. B.1. Redshift evolution of the Global 21-cm signal and the corresponding power spectra ($k \sim 0.1$ h/cMpc) for different $f_{*,0}$, keeping $f^{\rm SF}_{X,\rm esc}$ fixed at 1.0.

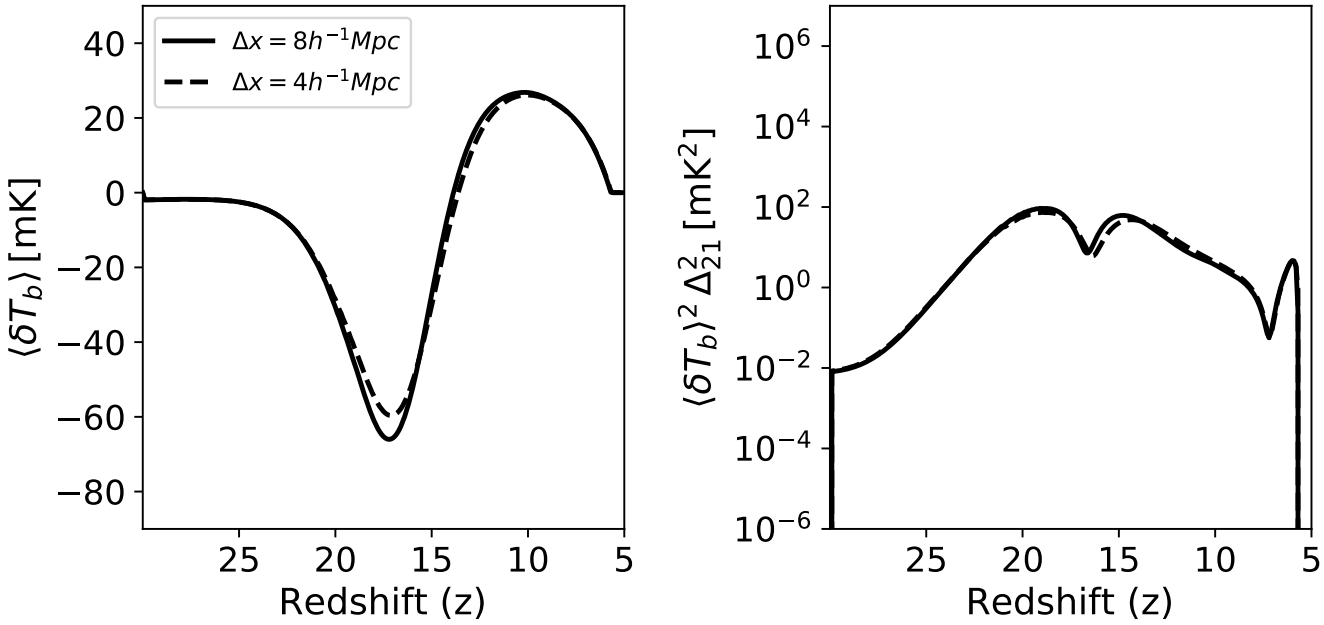

Fig. C.1. Comparison of 21cm observables between two resolutions ($\Delta x = 4\ h^{-1}$cMpc and $8\ h^{-1}$cMpc) of the simulation setup.